The Design and Characterization of a Co-Axial Electrodeless Magnetoplasmadynamic Thruster

Grace Zoppi,* Tate M. Gill,† Christopher L. Sercel,‡ and Benjamin A. Jorns§

University of Michigan, Plasmadyamics and Electric Propulsion Laboratory, Ann Arbor, MI, 48109

The design of a coaxial electrodeless magnetoplasmadynamic (E-MPD) thruster that employs current generation via a rotating magnetic field (RMF) is presented. Previous experimental and modeling work conducted on a conical RMF-driven thruster highlighted the need to enhance the applied and RMF field strengths to increase thruster efficiency. To facilitate these changes, a coaxial thruster configuration, similar to a Hall thruster, is designed. Specifically, a 6-kW class Hall thruster is reconfigured to support the RMF drive necessary for thrust generation. The design incorporates high-permeability ferrite materials to confine magnetic flux to the channel region, thereby mitigating eddy current power losses. The RMF antennas are also reconfigured for operation at a higher RMF frequency of 1.8 MHz. Using a calibrated fluid model to predict the performance of the coaxial configuration, the efficiency downstream of the power processing unit is predicted to be ~40%. This contrasts with the conical E-MPD prototype that achieved only 13.5%. These performance gains are shown to be attributed to an increased mass utilization and reduced heat lost to the thruster's backwall and exit.

I. Nomenclature

B_0	=	Applied Magnetic Field Magnitude
B_ω	=	Rotating Magnetic Field Magnitude
e	=	Electron Charge
m_e	=	Electron Mass
n_n	=	Neutral Number Density
n_p	=	Plasma Number Density
R	=	Thruster Radius
$v_{e,\theta}$	=	Azimuthal Electron Velocity
ζ	=	Collisional Drag
v_{ei}	=	Electron-Ion Collision Frequency
v_{en}	=	Electron-Neutral Collision Frequency
$\langle \sigma_i v_e \rangle$	=	Ionization Reaction Rate Coefficient for a Maxwellian Plasma
ω	=	Rotating Magnetic Field Angular Frequency

II. Introduction

Applied Field Magnetoplasmadynamic (AF-MPD) thrusters are an enabling technology for the next generation of in-space propulsion [1]. Their key benefits include high-power operation over 100 kW, high specific impulse in the range of 2000-9000s [2], and an inherently higher thrust density than other state of the art electric propulsion devices [3, 4]. Despite these advantages, a major outstanding challenge with AF-MPDs is thruster lifetime due to high levels of electrode erosion [5–8].

The electrodeless MPD (E-MPD) thruster is intended to address this problem while still offering the performance benefits of an AF-MPD. In this concept, a rotating magnetic field (RMF) is employed to electrodelessly induce an

---

*PhD Candidate, Department of Aerospace Engineering, University of Michigan, Ann Arbor, MI. AIAA Student Member.

†Assistant Research Scientist, Department of Aerospace Engineering, University of Michigan, Ann Arbor, MI. AIAA Young Professional Member.

‡Postdoctoral Fellow, Department of Aerospace Engineering, University of Michigan, Ann Arbor, MI. AIAA Young Professional Member.

§Associate Professor, Department of Aerospace Engineering, University of Michigan, Ann Arbor, MI. AIAA Associate Fellow.

azimuthal current in a annular plasma that then can interact with an applied radial field, generating the same type of Lorentz force exhibited by AF-MPDs. In contrast to the AF-MPD, where this azimuthal current is driven by a DC applied electric field between electrodes, the RMF has minimal electrical interaction with the plasma. This concept in principle thus allows for the same propulsive benefits of an AF-MPD but with an extended lifetime.

The idea for this electrodeless MPD enabled by RMF current is inspired in large part by the extensive body of previous work on RMF pulsed inductive plasma thrusters [9–16]. In these devices, the RMF was employed to repeatedly generate and accelerate, via a Lorentz force interaction, high density plasmoids. The electrodeless MPD concept differs from these previous devices in that the RMF is applied continuously (a continuous wave, CW, mode) to generate a steady-state current that interacts with an applied field to produce Lorentz force (similar in principle to the AF-MPD). The motivation for this paradigm change, in part, stems from the fact that our recent work has shown that a CW mode of operation inherently can achieve higher total efficiencies [17]. This is a result of the lower plasma densities for a given power level in the CW mode, which are orders of magnitude smaller than in a pulsed mode. This reduced density eliminates the radiative loss processes that we have shown cripple the efficiency in pulsed RMF systems [18].

With that said, while we have shown the CW-mode improved overall efficiency for an RMF device, the results we have obtained to date (efficiency of $\sim 3\%$) are notably low compared to more mature state-of-the-art electric propulsion devices. This invites the question as to whether there may be strategies to improve the performance. In light of the advantages of an electrodeless RMF concept—particularly given its potential to address outstanding challenges with AF-MPD lifetime—the need is thus apparent for the design and development of a new E-MPD test article.

To that end, this paper is organized in the following way. In Sec.III, we describe the operating principles of the E-MPD thruster. We also elaborate on the experimental and modeling results that serve to motivate the design of the new E-MPD test article. Then in Sec.IV, we outline the construction and highlight the performance predictions of the new test article in Sec.V. We conclude with Sec.VI, which provides a discussion on model assumptions and their effects on performance predictions.

III. Motivation for the Electrodeless Magnetoplasmadynamic Thruster

While we previously have explored the concept of using a CW-mode RMF for plasma acceleration [17], this prototype exhibited prohibitively low performance. In order to motivate our new design, we thus outline here the key drivers that we suspect resulted in the thruster's low efficiency. To this end, we first describe the principle of operation of this previous approach to a continuous wave RMF thruster, which is based on a conical geometry. We then explore the limitations of the conical RMF driven thruster by reviewing our experimental and modeling findings. We conclude this section by identifying strategies to mitigate dominant loss processes and improve thruster efficiency.

A. Principle of Operation of a Continuous Wave Rotating Magnetic Field Thruster

Fig.1a shows a conical version of the RMF thruster geometry we previously investigated. It consists of three-phase RMF antennas surrounding a plasma-bounding structure. The walls of the plasma bounding cone are roughly conformal to the applied magnetic field which is supplied by external solenoids.

The thruster operation begins by injecting a seed plasma into this volume. The RMF antennas then fire sequentially in a manner analogous to the action of the stators in an induction motor to create the RMF. This, in turn, drives an azimuthal electron current, and as more electrons are entrained, more particles are ionized. The time average azimuthal electron velocity, derived in Ref. [16] under the assumption of a zero radial pressure gradient, is mathematically represented as

$$v_{e,\theta} = \frac{\omega R}{1 + 2(B_0^2 + \zeta^2)/B_\omega^2}. \tag{1}$$

Here, ω is the angular frequency of the rotating magnetic field, R is the radial distance from thruster center-line, B_0 is the magnitude of the applied DC magnetic field, B_ω is the magnitude of the rotating magnetic field, and $\zeta = m_e(\nu_{ei} + \nu_{en})/e$ is a collisional drag term. The collisional drag term is dependent on the electron-ion collision frequency, ν_{ei}, and the electron-neutral collision frequency, ν_{en}. Fig.1b shows that a Lorentz force interaction between the azimuthal electron current and the radial magnetic field accelerates electrons out of the thruster. Ions then follow through an ambipolar electric field resulting in thrust generation.
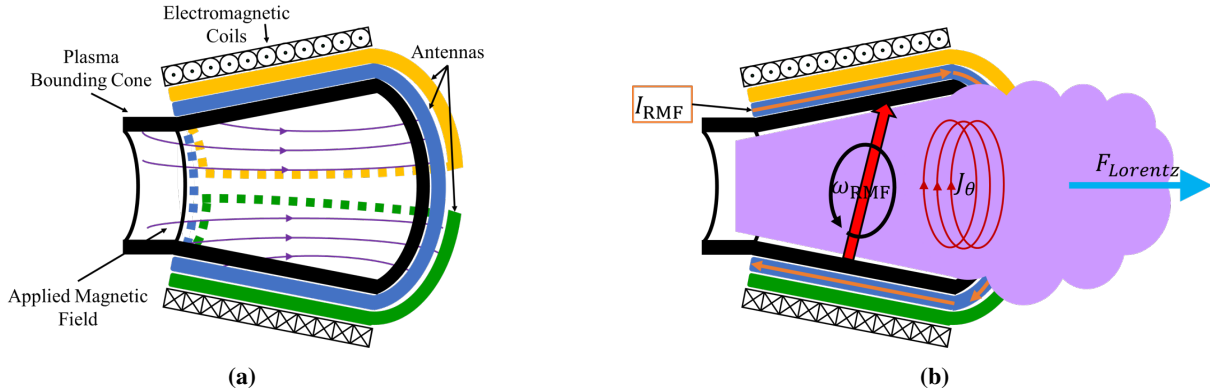

Fig. 1 **Illustrations of (a) the key elements of the CW RMF thruster and (b) the internal processes that result in thrust generation.**

B. Review of Performance Analysis of the First Version of a Continuous Wave RMF Thruster

1. Description of Test Article and Experimental Results

In our most recent test campaign, we characterized the performance of the RMF v3 thruster [17], shown in Fig.2, that is based on the principle of operation outlined in the previous section. As shown in the image, the main structure of the RMF v3 is a conical glass plasma bounding cone. The three-phase antennas, made from stranded 8 AWG copper core wire, are wrapped around the exterior of this structure. Tuning capacitors are used to produce a specific RMF frequency of 413.2 kHz. Additionally, solenoids provide the applied DC magnetic field, and the seed plasma necessary for initial plasma ionization is provided by a LaB_6 cathode.
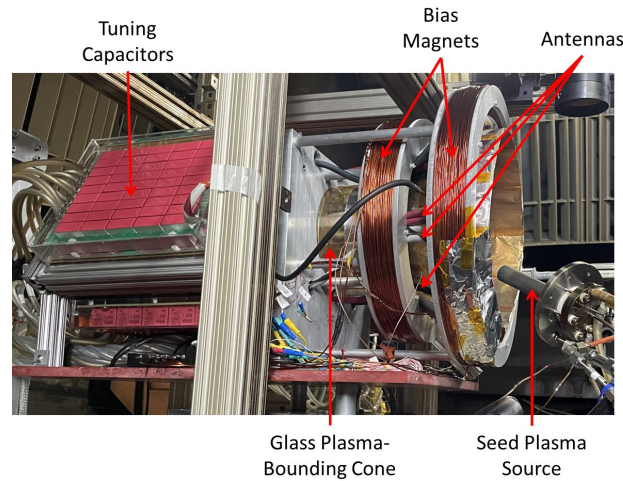

Fig. 2   The RMF v3 test article.

With our previous test article, we performed a parametric experimental analysis of the impact of flow rate, magnetic field strength, and RMF field amplitude on performance in the CW mode [15]. While we were able to demonstrate that key features–such as applied field strength–translated generally to increasing performance, overall we found that the total efficiency of the system in this parameter space was maximized at less than 3%. This occurred at the operating conditions of a 20.5G RMF magnitude, a 80G to 120G applied bias field, a xenon flow rate of 275 sccm, and 14.6 to 16 kW average PPU power. This poor result invited the follow on question as to why this performance was so low, which we subsequently addressed through a model-based study.

2. Description of the Reduced Fidelity Model for Analyzing Efficiency Modes

To characterize the performance of the prototype RMF CW thruster, we previously developed a quasi-1D model and verified it using experimental data for thrust and the power coupled into the plasma of the RMF v3 thruster. This model is described in detail by Ref. [19]. In brief, the fluid model represents the RMF v3 thruster as a quasi-1D geometry by splitting the computational domain into cylindrical cells of increasing radii. It includes a continuity equation for the neutral and plasma species including the effects of ionization and wall recombination events. The equation for ion momentum also accounts for ionization and wall recombination events. We note here that for this work, we have revised the model to include a power balance equation that assumes isothermal electrons. The derivation of this updated power balance equation is provided in the appendix.

As the model is a quasi-1D representation of an inherently 3D thruster there are a number of free parameters that must be tuned so that the model outputs match experimental data for a given operational condition. Table 1 summarizes the model free parameters, their physical bounds, and there associated dependencies within the model. There is a free parameter for the magnetic field wall confinement factor, β_m, that affects the rate at which the plasma species is lost to the walls, Γ_{wall}. The effect of self-induced magnetic fields screening out the applied field [15], is encapsulated in the induced magnetic field free-parameter (σ). This affects the magnitude of the azimuthal electron velocity, $v_{e,\theta}$. The power loss due to heating of the backwall (P_{bw}) and frozen flow at the thruster's exit (P_{exit}) are affected by the heat flux at the upstream and downstream boundary, q_1 and q_2, respectively. Both parameters are unitless as they scale

proportionally to the model calculated upstream and downstream thermal energy fluxes. Finally, the plume divergence angle, θ_d, captures how collimated the plasma plume is at the thruster exit and effects the divergence efficiency (η_d) and thrust predictions (F_T).

Free Parameter	Symbol	Physical Bounds	Units	Dependent Calculation
Magnetic Field Wall Confinement Factor	β_m	$0 \rightarrow \infty$	G^2	Γ_{wall}
Induced Magnetic Field Factor	σ	$0 \rightarrow \infty$	$-$	$v_{e,\theta}$
Backwall Heat Flux	q_1	$0 \rightarrow \infty$	$--$	P_{bw}
Outflow Heat Flux	q_2	$0 \rightarrow \infty$	$--$	P_{exit}
Divergence Angle	θ_d	$30 \rightarrow 60$	deg	η_d & F_T

Table 1   Summary of the model free parameters that must be learned in order to calibrate the model.

3. Model-based Insights Into Low Performance

For consistency, we use the same data set from Ref. [19] for model calibration, ensuring that the model predictions for thrust and the power coupled into the plasma align with the experimental values at identical applied field configurations. In order to calibrate the model, we follow the method outline in Ref. [19]. We can then leverage the calibrated model to characterize the efficiency modes of the v3 thruster.

Figure 3 presents the mass utilization, divergence, and plasma efficiency for the bias magnetic field configuration with 35G radially and 110G axially. Experimentally thruster efficiency reached a maximum of 2.56% at this magnetic field configuration. The mass utilization captures how efficiently neutral particles are ionized. The divergence efficiency is a measure of how collimated the plasma plume is at thruster exit. The plasma efficiency is the ratio of the useful momentum power to the total power coupled into the thruster via the RMF antennas. The product of these three efficiency modes is the post-coupling (downstream of the power processing unit) efficiency. The total thruster efficiency is thus the product of the post-coupling efficiency and the coupling efficiency. As the coupling efficiency measures how much of the power processing unit (PPU) power is coupled into the plasma, it is thus dependent on the PPU design itself and agnostic to the model. Overall, plasma efficiency emerges as the dominant factor contributing to the v3 thruster's low overall efficiency consistent with experimental measurements [16].

Figure 4 illustrates how the plasma power is divided into useful momentum power and the loss processes for the best-performing case from the RMFv3. The primary power losses in the v3 thruster are attributed to heat loss to the backwall and frozen flow losses at thruster exit. Physically, this suggests that the thermal energy in the plasma is poorly confined.

In turn, these results provide insight into possible strategies on improving thruster performance. Chief among these is a need to eliminate unwanted heat loss to the backwall and frozen flow losses at thruster exit. This in principle can be achieved by employing a stronger applied field to enhance the overall useful momentum power. We also note that increasing the RMF field magnitude will enhance the Lorentz force acceleration, also potentially boosting overall performance. We revisit this strategy in the following section.
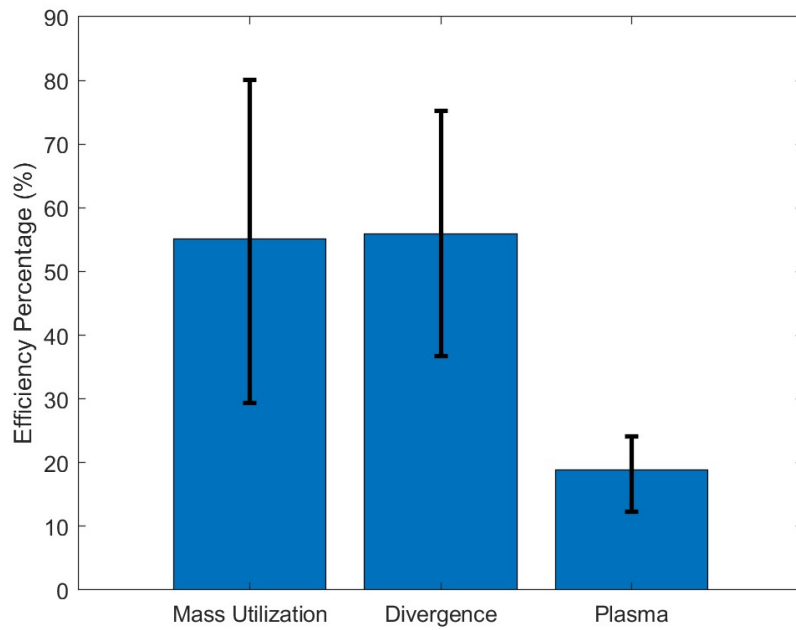
Fig. 3   Model predictions of the mass utilization, divergence, and plasma efficiencies of the RMFv3 thruster operating at its peak efficiency.
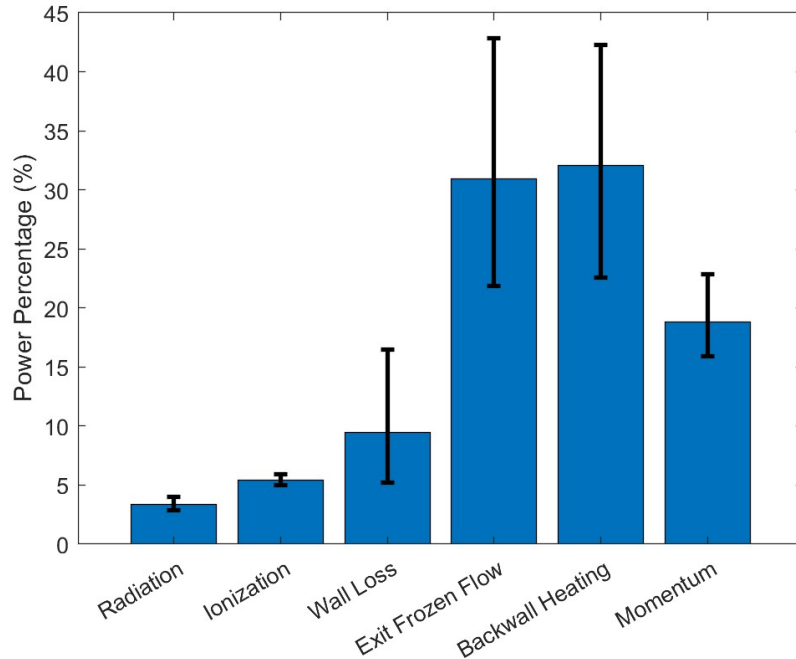

Fig. 4   Model predictions of the power fractions of the RMFv3 thruster operating at its highest performance point with an applied radial magnetic field of 35G.

6

C. Design Strategies to Address Limitations of the Baseline RMF thruster

From the experimental and modeling results we found that in order to increase the efficiency of the thruster, the applied and RMF field strengths must be increased. One potential solution to achieve these design requirements is to redesign the RMF driven thruster to an annular geometry. Fig.5 shows the notional concept in which electromagnets energize inner and outer magnetic cores providing a magnetic field across the annular discharge channel through which propellant is axially injected.

The switch from air-core applied field solenoids in the previous v3 test article to magnetic cores in this coaxial design will lead to substantially higher bias magnetic fields, with expected values as high as 300 G across the channel. Additionally, the RMF antennas can be embedded on the inner and outer sides of the channel. The close proximity of the two sides of each antenna (3 cm versus the ~10-15 cm in the RMF v3) will promote a stronger RMF field strength without the need to increase PPU power. An annular geometry would also eliminate "dead" regions in which little azimuthal electron current is driven. This occurs at smaller radii near the thruster center (described by Eqn. 1). The annular geometry confines the flow to a larger overall radius without requiring the thruster to be prohibitively large, enhancing the effective use of the propellant in the device. Through these design advantages, we expect an improvement in overall thruster efficiency.
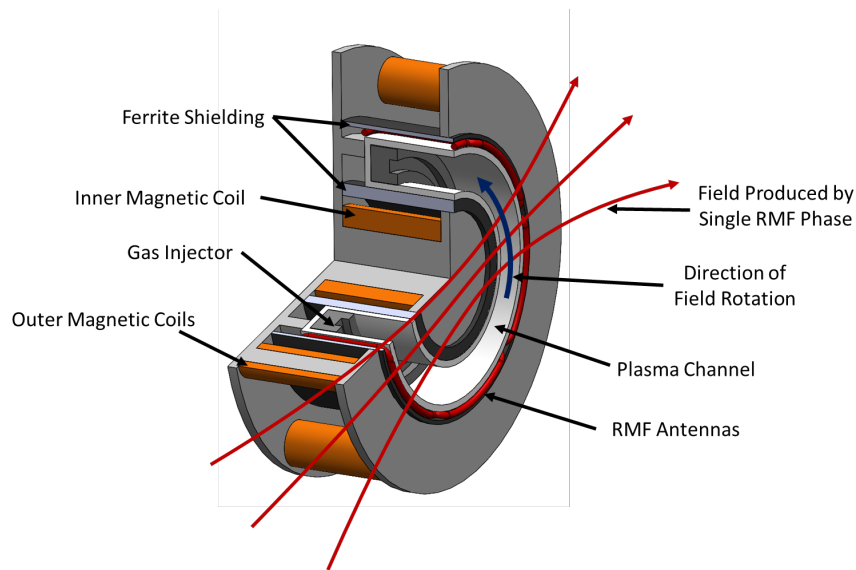

Fig. 5   Cross-sectional view of the coaxial E-MPD thruster concept.

IV. E-MPD Thruster Design

In light of the design considerations we outlined in the preceding, our next design iteration, which is outlined in this paper, is to attempt to implement an annular configuration. As a proof-of-concept, we have recycled the magnetic circuit and flow manifold from a Hall effect thruster, which as seen from Fig. 5 has a geometry well-suited to enabling the annular version of the RMF device. To this end, we have baseline the H6, 6-kW system [20–22], which we have in house in our laboratory. This device consists of a boron nitride discharge channel and a magnetic circuit consisting primarily of iron. A center-mounted hollow cathode sources electrons, and gas flow is injected axially through the discharge chamber from an upstream gas manifold. In this section we start by describing the necessary design changes to the H6 to facilitate RMF drive. We then overview the properties of the RMF driving circuit. We conclude with a simulated analysis of the anticipated RMF properties.

A. Design Modifications to the H6

1. Antenna Geometry

The design of the three-phase antennas, which fire sequentially to generate the RMF, must be re-conceptualized to fit within the geometric constraints of the notional H6 thruster. We thus proceed by removing the inner and outer screens, components which primarily serve to provide fine control over magnetic shaping in the channel in the nominal H6 configuration. These features are not necessary for this preliminary proof of concept.

Figure 6 illustrates how the antennas fit within the cylindrical confines of the coaxial geometry, encompassing the outer diameter of the discharge channel. The redesigned antennas each consist of 14 total turns of wire, and antennas of the same color fire simultaneously but in opposite polarities. Instead of the stranded 8 AWG copper core wire used in the RMF v3 thruster, the new antennas are made from Litz wire. The braided strands of Litz wire minimize parasitic losses by reducing the AC power skin effect.
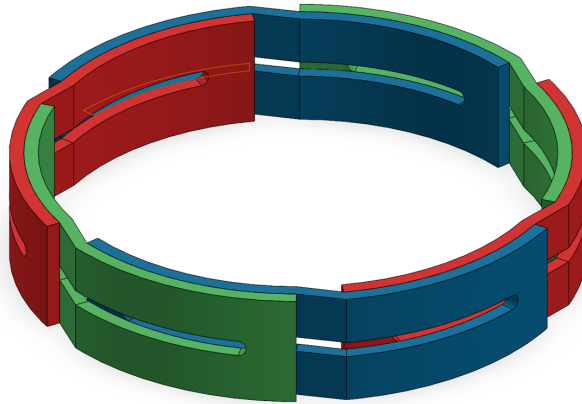

Fig. 6   A 3D visualization of the cylindrical three phase RMF antennas. Antenna pairs which are linked in series are color coded.

2. Ferrite Shielding

The magnetic circuit of the H6 thruster is made of iron, a material with high relative permeability, which in principle would be beneficial to constrain the RMF magnetic field flux to the channel region. However, iron also has a high electrical conductivity causing the formation of eddy currents at the RMF frequencies of interest. These eddy currents couple power into the thruster body leading to high parasitic losses. In an effort to avoid these effects, we placed ferrite around the thruster discharge channel in-between the walls of the discharge chamber and antenna. This material has a high magnetic permeability and a low electrical conductivity, which is conducive to conducting magnetic flux at high frequency with minimal losses. The flux in turn is shunted radially across the channel but around the iron pieces, thus avoiding penetration losses.

In practice, to shield the iron on the outer diameter of the channel, we line the outer diameter of the RMF antenna configuration with flexible ferrite sheets. These sheets, which are commercially available off-the-shelf, are advantageous

due to their design flexibility. Each sheet is comprised of a PET film layer, a ferrite layer, and an adhesive backing, and at the targeted operating frequencies, the ferrite sheets achieve a nominal relative permeability of 220 [23]. On the inner diameter of the channel, we shield the central iron components with additional layers of flexible ferrite sheets stacked around a supporting structure.

3. Aluminum Structure

The flexible nature of the ferrite components necessitates a supporting structure to maintain their shape. We chose aluminum for this purpose because of its low cost, ease of manufacturing, and adaptability. Figure 7 illustrates how we contain the ferrite sheets with an aluminum mounting fixture. The ferrite sheets replacing the inner screen are wrapped around an aluminum housing, while the ferrite sheets replacing the outer screen are enclosed by the aluminum framework. The outer screen replacement structure also has a cavity to house the RMF antennas.
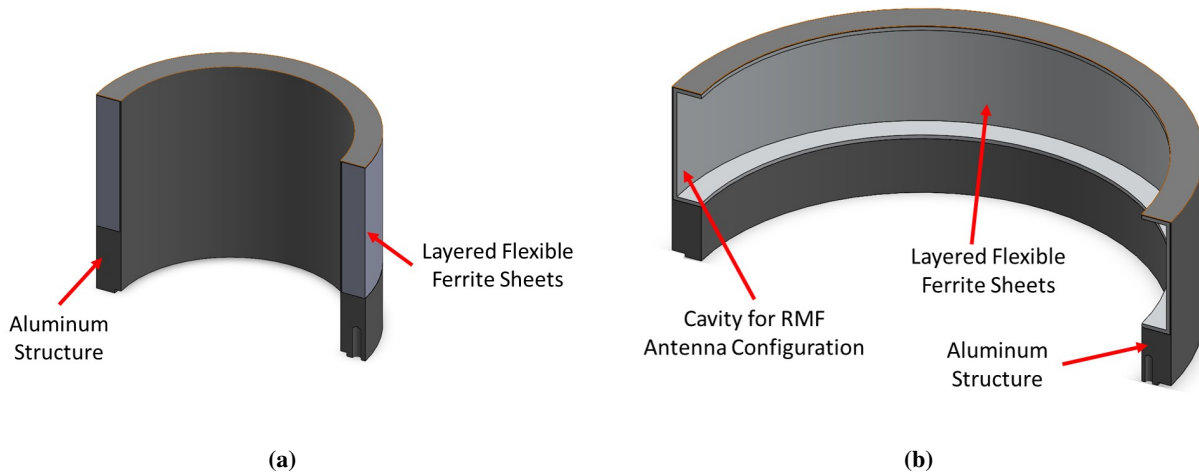

(a)

(b)

Fig. 7   A CAD rendering of (a) the inner screen replacement and (b) the outer screen replacement. The outer structure has a cavity to house the cylindrical RMF antenna configuration.

B. RMF Properties

In addition to design changes we have made to the H6, for this effort, we also have revised our approach to the RMF processes. In the RMFv3 test campaigns, we employed a 400 kHz RMF, a limitation which stemmed from the constraints of the power processing unit (PPU). For the E-MPD, we intend to operate the new PPU at higher frequencies compared to the RMF v3 PPU. The motivation for this results from the underlying theory of RMF (per Eq. 1), in which increased RMF frequencies facilitate increased azimuthal velocities and thus larger azimuthal currents. To first order, this in turn will lead to enhanced Lorentz force and thus increased efficiency. To allow for this higher frequency implementation, we have revised the PPU design to allow for faster switching of the gate drivers.

C. Finite Element Analysis Simulation

We present, in this section, a simulated analysis of the anticipated RMF field strength in the new design. To make this prediction, we performed a 2D finite element analysis (FEA) simulation in COMSOL on an $R - \theta$ cross-section of the thruster channel, in which the antennas were modeled as solid copper blocks and the ferrite sheets as solid cylindrical structures. A smaller scale 2D-FEA simulation, comprised of stacked ferrite sheets, demonstrated that the PET and adhesive layers in the sheets changed the predictions of the RMF strength by ~3%. Thus, both the inner and outer ferrite structures were modeled as solid cylindrical shells, each followed by a thin cylindrical shell of aluminum.

To sustain the rotating magnetic field, the antennas fire 120° out of phase with one another. When the primary antenna reaches a maximum current amplitude, the secondary antennas are each at half of the maximum current. The maximum current through the antennas is limited by PPU constraints, rated to a peak current of 50 A [24]. Therefore, using the 14-turn antenna configuration, the primary antenna drives 700 A-turn, while each secondary antenna drives

9

350 A-turn. The increased number of antenna turns in the coaxial E-MPD design, compared to the RMF v3, means that we can operate at a larger amp-turn value without prohibitively large currents through the antennas.

Fig. 8a, 8b, and 8c shows snapshot images of the results of the time-resolved FEA simulation demonstrating the rotation of the RMF as each antenna pair fires in sequence. As can be seen, the RMF field lines are primarily radial, the RMF magnitude is peaked across channel, and the magnetic flux is shunted around the channel. The simulated RMF magnitude is utilized to inform performance predictions for the E-MPD thruster.
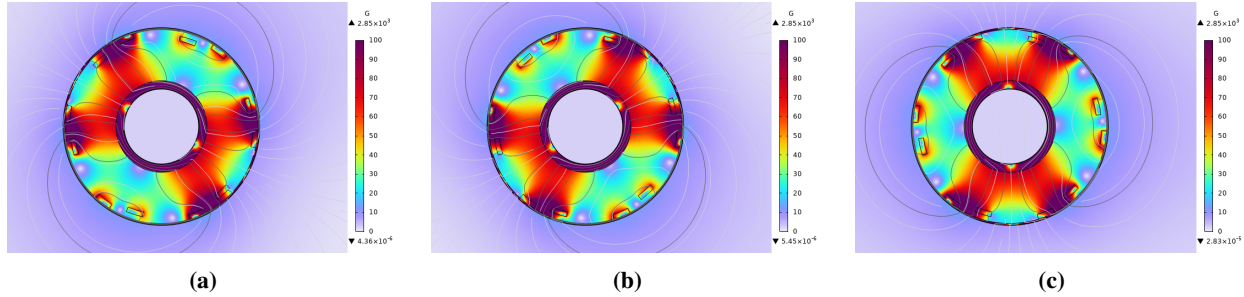

(a)   **(b)**   **(c)**

Fig. 8 **2D FEA simulation results of RMF field and magnitude in E-MPD design with the anticipated maximum PPU current to the coils as each antenna pair fires sequentially. The cross-section of the RMF antenna are represented by rectangles on the outer diameter of the channel region.**

V. E-MPD Model-Based Performance Predictions

Now that we have outlined the proposed geometry, we attempt here to assess the anticipated improvements to performance from this design. To this end, we have revised our model originally described in Ref. [19] to accommodate the modified annular geometry. These changes are detailed in the appendix.

Armed with this updated model, we used the geometric parameters of the H6 thruster and the posterior values of the model parameters inferred from the RMF v3 data set (Sec.III.B.2)to generate performance predictions for the coaxial E-MPD thruster. We set the RMF field strength to the maximum value possible in the channel (60 G) as anticipated from the simulations detailed in the previous section. We then parametrically varied the operating conditions of the E-MPD thruster, following the optimization approach described in Ref. [19] to identify the best-performance test conditions.

Following this prescription, we found the optimized xenon flow rate is 275 sccm – consistent with the operational conditions of the v3 thruster. The optimized average applied radial field strength was 232 G. The input power at these design conditions was 6250 W. Subject to these values, we show in Figure 9a the predicted post-coupling (downstream of the PPU) efficiency of the coaxial E-MPD thruster to be 40%, a significant improvement over the experimental efficiency of 13.5% reported for the v3 thruster [17]. We show the results of the full efficiency model predictions in Fig.9a for mass utilization, divergence, plasma, and the post-coupling efficiency. We discuss these individual modes in the following subsections.

A. Mass Utilization

As shown in Fig.9a the model predicts the mass utilization efficiency to be 92%, a substantial increase from the 55% model prediction of the RMF v3 thruster. We suspect this gain is primarily due to enhanced ionization in the E-MPD design. The reduction of the cross-sectional area (20% of the RMFv3) in the annular geometry of the E-MPD leads to increased neutral particle densities for a fixed flow rate. Since the ionization rate scales with neutral density [25], we thus anticipate that the ionization and thus mass utilization for the E-MPD will increase commensurately.

B. Divergence Efficiency

The divergence efficiency remains unchanged between the v3 and coaxial E-MPD thrusters because the plume divergence angle is a free parameter learned from the RMF v3 dataset. Currently, no formulaic expression exists to predict the divergence angle based on operating conditions, but this efficiency likely represents a lower bound for the coaxial E-MPD's performance. We speculate that the coaxial design will produce a more collimated plasma plume compared to the conical geometry of the v3 thruster, which had a mean divergence angle of 42°. This is because the

coaxial geometry has an increased radial bias field, which will facilitate increased Lorentz force acceleration in the axial direction, and if the radial force balance remains similar to the RMF v3, will reduce divergence losses.

C. Plasma Efficiency

At a selected input power of 6250 W, comparable to the operational condition of the RMF v3 thruster data used to calculate the model free parameters, the predicted plasma efficiency (the conversion of input power to the plasma to directed kinetic energy) is 66% – a marked improvement over the 20% estimated for the RMFv3.

In order to illustrate the key drivers for this performance improvement, we show in Figure 9b the modes in which the plasma power can be coupled. As can be seen in Figure 4, a key driver for improved performance is that more energy is proportionally coupled into momentum power (Lorentz force) rather than into electron heating. We suspect this can attributed to both the increased RMF and applied field magnitudes in the annular E-MPD thruster.

We also see from Figure 9b that the losses to walls and backwall heating are proportionally reduced. This can be attributed to two features. First, even though the H6 is an annular design, the actual H6 channel and diameter are smaller than the plasma bounding cone of the RMF v3 thruster. This results in a wall area 78% that of the RMF v3 thruster, thus allowing for reduced wall losses. At the same time, the applied magnetic fields in this thruster are a factor of three higher, providing for reduced transport to the backwall and in turn reducing power lost due to heating of the backwall.

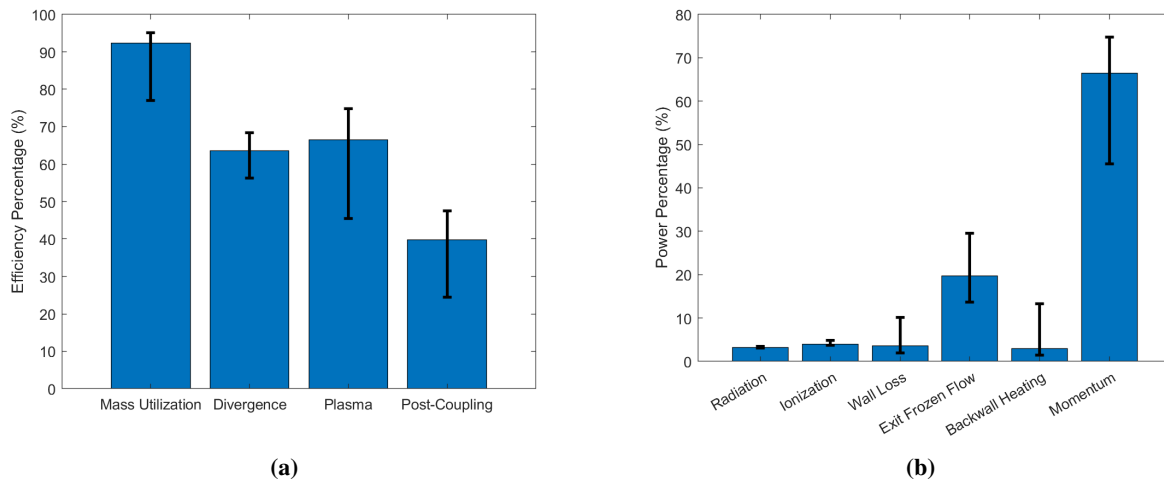**(a)**   **(b)**

Fig. 9   Model predictions for the (a) coaxial E-MPD's efficiency modes and (b) the fractional plasma power contributions. The operational conditions chosen for these performance predictions were an applied radial field of 232 G, a plasma power of 6250 W, and a xenon flow rate of 275 sccm.

In summary, from the preceding analysis, we have shown that we anticipate the E-MPD design will exhibit at least a 3x improvement in efficiency compared to the baseline RMFv3. These advantages in large part can be attributed to the ability of this design to support increased RMF and applied field magnitudes.

VI. Discussion

We discuss in this section the limitations of the computational model and the effects on performance predictions. In particular, the key caveat to our analysis is that we have explicitly assumed that the model parameters we calibrated from the RMFv3 can apply to this new design. The validity of extending these conditions to this new design has not been established.

For example, we have largely neglected the role of coupling efficiency, which is a key driver for overall performance. We have instead assumed that the coupling efficiency is the same between the RMF v3 and the coaxial E-MPD thruster. As such, we assumed that we are able to couple the same amount of power into both devices. In practice, the amount of coupled plasma power is determined by the PPU's coupling efficiency. This efficiency depends on the resistance of the RMF antennas, circuit elements of the PPU, and the plasma resistance. The plasma resistance in turn is a function of both the applied and RMF field strengths, such that the coupling efficiency, and plasma power, is not strictly agnostic to the model. With that said, previous modeling work conducted in Ref. [16] indicated that increasing the RMF magnitude at a given coil current will increase the power coupled into the plasma. We therefore expect that the new PPU and coaxial configuration may be able to support similar or even higher levels of power into the discharge from the power processing unit.

Another major model limitation stems from using the same magnetic field confinement factor (a model free parameter that captures the degree to which the field inhibits plasma flux to the walls) for the E-MPD as with the RMFv3. In practice, however, the applied magnetic field strength and shape differs substantially between the two geometries, which in turn likely will result in different effective confinement factors. Optimistically, we anticipate that the confinement factor will be even further improved in the E-MPD given that the H6 magnetic circuit is designed to help reduce flux to the channel walls. This would imply that our performance predictions are under-predictions.

As a final note, we make the caveat that the ferrite sheets may begin to less effectively constrain the field to the channel region as they saturate at the baselined field strengths. To verify and compare the RMF strength to the simulation predictions, we will generate an experimental magnetic field map of the RMF. We will then be able to compare this magnetic field map to our simulation results in order to generate updated E-MPD performance predictions.

With these limitations in mind, while our use of the model parameters from the RMFv3 has been a necessary step in order to facilitate our model analysis, the next step in practice is to refine the model based on experimental measurements from the actual E-MPD. Armed with these results, we will not only be able to more definitely assess performance losses but in turn leverage this updated model to further refine and optimize the E-MPD.

VII. Conclusion

We explored in this study the motivation, design, and performance predictions of a coaxial E-MPD thruster. Our proof-of-concept approach is based on adapting a Hall effect thruster magnetic circuit and channel to support an RMF-current drive. The motivation for this design is that our previous results on an RMF test article, using a CW-mode RMF, showed that the Lorentz force acceleration and plasma confinement are prohibitively low. The annularly-configured E-MPD design overcomes these challenges by allowing for stronger RMF and applied magnetic fields. We thus outlined the design and presented magnetic simulations that demonstrate the ability to support higher RMF and applied field strengths. We then in turn leveraged a reduced-fidelity model to generate predictions for the performance of this device. Overall, we have shown that the design changes outlined led to a post-coupling efficiency of 40%—-a factor of three increase from the RMF v3 thruster's post coupling efficiency of 13.5%. These improvements in large part stem from enhancements in mass utilization and plasma efficiency. The design advancements outlined in this work highlight the coaxial E-MPD thruster's potential to achieve higher efficiency, establishing it as a promising candidate for high-power electric propulsion applications.

Appendix

1. New Power Balance Equation

One of the model limitations presented in Ref. [19] was a result of neglecting heat flux, leading to very high predictions of electron temperatures. Namely, the model predicted a steep axial gradient in the electron temperature resulting in a predicted an electron temperature of 95 eV at the exit plane for the largest applied field strength. However, we do not believe this to be physical because secondary inelastic collisional losses will occur, limiting the overall electron temperature. To more accurately predict electron temperature, we now assume isothermality of the electron

fluid as the axial applied magnetic field will serve to thermalize the electrons within the thruster domain. The model has thus been updated to include a power balance equation that solves for a single consistent electron temperature across the entire axial domain. For comparison with experimental data, the electron temperatures at specific operating conditions must be determined through a Bayesian inference process. When using the model for performance predictions, the code iteratively adjusts the electron temperature to ensure that the power coupled into the plasma matches the power calculated by the model. The calculation of this temperature is based on the following power balance equation,

$$P_p = P_{mom} + P_{exc} + P_{wall} + P_{ion} + P_{bw} + P_{exit}, \tag{2}$$

where P_p is the power coupled into the plasma. Respectively, P_{exc}, P_{wall}, P_{ion}, P_{bw}, and P_{exit} represent the power loss due to excitation, wall recombination, ionization, backwall heating, and frozen flow at the thruster exit.

To calculate the power losses internal to the domain (excitation, wall, and ionization losses) the power lost in each computational cell is accounted for by taking the summation over the entire length of the thruster. This is calculated in the same way as done previously in Ref. [19]. The power loss due to heating of the thruster's backwall, P_{bw}, and frozen flow at thruster exit, P_{exit}, are mathematically described as

$$P_{bw} = \left(\frac{5}{2} + q_1\right)\left(T_e n_p u_p A\right)_{bw} \tag{3}$$

and likewise

$$P_{exit} = \left(\frac{5}{2} + q_2\right)\left(T_e n_p u_p A\right)_{exit}. \tag{4}$$

This new power balance equation necessitates two new free parameters. These free parameters, q_1 and q_2, represent the residual thermal energy loss due to heat flux at the domain boundaries. Specifically, q_1 modulates the power loss to the backwall, and similarly q_2 alters the power loss to frozen flow at the thruster exit. The upstream boundary for the plasma species is modeled to match sheath criteria, such that the $u_{p,bw} < 0$, as the plasma species is flowing upstream through the sheath into the backwall.

A. Model Updates for a Coaxial Geometry

For a coaxial configuration, the geometry of the cell is altered such that the volume, V, of a computational cell is now

$$V = \pi(R_2^2 - R_1^2)dx \tag{5}$$

where R_2 and R_1 are the outer and inner radius of the channel respectively, and dx is the width of the cell. The total surface area, SA, of the cell considering both the inner and outer wall surface is

$$SA = 2\pi(R_2 + R_1)dx, \tag{6}$$

and the cross-sectional area, A, of a cell is

$$A = \pi(R_2^2 - R_1^2). \tag{7}$$

These geometric terms directly effect the flux calculations in the neutral continuity, ion continuity, ion momentum, and internal power loss processes. The other pertinent update in the coaxial configuration is to the wall recombination rate term (Γ^{wall}). This is altered to,

$$\Gamma^{wall} = 0.6 \frac{2}{R_2 - R_1} \langle n_i \rangle \sqrt{\frac{k_b \langle T_e \rangle}{m_i}} D_B,$$

to account for wall losses on both the inner and outer walls of the channel. Here, k_b is the Boltzmann constant, T_e (K) is the electron temperature, and D_B is a magnetic diffusion coefficient. The magnetic diffusion coefficient is expressed as

$$D_B = \beta_m exp\left(-B_{0,\parallel}^2\right), \tag{8}$$

where β_m is an effective magnetic confinement factor and $B_{0,\parallel}$ is the tangential component of the applied magnetic field to the walls. This formulation is based on the assumption that the transport across the magnetic field lines is dictated by classical diffusion [26].

Acknowledgments

References

[1] National Academies of Sciences, E., and Medicine, *Space Nuclear Propulsion for Human Mars Exploration*, The National Academies Press, Washington, DC, 2021. https://doi.org/10.17226/25977, URL https://nap.nationalacademies.org/catalog/25977/space-nuclear-propulsion-for-human-mars-exploration.

[2] Kodys, A., and Choueiri, E., *A Critical Review of the State-of-the-Art in the Performance of Applied-Field Magnetoplasmadynamic Thrusters*, 2012. https://doi.org/10.2514/6.2005-4247, URL https://arc.aiaa.org/doi/abs/10.2514/6.2005-4247.

[3] Lev, D. R., "Investigation of Efficiency in Applied Field MagnetoPlasmaDynamic Thrusters," Ph.D. thesis, Princeton University, 2012.

[4] Centrospazio, A. S. P. A., and Gherardesca, A., "FUNDAMENTAL SCALING LAWS FOR ELECTRIC PROPULSION CONCEPTS Part 1 : Hall Effect Thrusters," 2003. URL https://api.semanticscholar.org/CorpusID:115150864.

[5] Wu, P., Wang, Y., Li, Y., Wang, B., Zhang, K., Tang, H., and Cao, J., "Cathode erosion site distributions in an applied-field magnetoplasmadynamic thruster," *Plasma Science and Technology*, Vol. 22, No. 9, 2020, p. 094008. https://doi.org/10.1088/2058-6272/ab9172, URL https://dx.doi.org/10.1088/2058-6272/ab9172.

[6] Sovey, J. S., and Mantenieks, M. A., "Performance and lifetime assessment of magnetoplasmadynamic arc thruster technology," *Journal of Propulsion and Power*, Vol. 7, No. 1, 1991, pp. 71–83. https://doi.org/10.2514/3.23296, URL https://doi.org/10.2514/3.23296.

[7] Jones, R. E., and Walker, E. L., "Status of large vacuum facility tests of MPD ARC thrustor," Tech. rep., NASA, Lewis Reserach Center, Cleveland, OH, January 1965.

[8] Tahara, H., Kagaya, Y., and Yoshikawa, T., "Performance and Acceleration Process of Quasisteady Magnetoplasmadynamic Arcjets with Applied Magnetic Fields," *Journal of Propulsion and Power*, Vol. 13, No. 5, 1997, pp. 651–658. https://doi.org/10.2514/2.5216, URL https://doi.org/10.2514/2.5216.

[9] Justin W. Koo, R. S. M., and Sousa, E. M., "High fidelity modeling of field-reversed configuration (frc) thrusters," Tech. rep., Air Force Research Laboratory, Edwards Air Force Base, CA, April 2017.

[10] Furukawa, T., Takizawa, K., Kuwahara, D., and Shinohara, S., "Electrodeless plasma acceleration system using rotating magnetic field method," *AIP Advances*, Vol. 7, No. 11, 2017, p. 115204. https://doi.org/10.1063/1.4998248, URL https://doi.org/10.1063/1.4998248.

[11] Kirtley, D., Pancotti, A., Slough, J., and Pihl, C., "Steady Operation of an FRC Thruster on Martian Atmosphere and Liquid Water Propellants," *48th AIAA/ASME/SAE/ASEE Joint Propulsion Conference & Exhibit*, 2012. https://doi.org/10.2514/6.2012-4071, URL https://arc.aiaa.org/doi/abs/10.2514/6.2012-4071.

[12] Weber, T. E., "The Electrodeless Lorentz Force Thruster Experiment," Ph.D. thesis, University of Washington, 2010.

[13] Chen, Q., Jia, Y., Sun, X., Lv, F., Geng, H., and Rao, B., "Analysis of azimuthal electron current driving by rotating magnetic field in field-reversed configuration electric propulsion," *AIP Advances*, Vol. 14, No. 11, 2024, p. 115207. https://doi.org/10.1063/5.0236397, URL https://doi.org/10.1063/5.0236397.

[14] Woods, J. M., "Performance of a Rotating Magnetic Field Thruster," Ph.D. thesis, University of Michigan, 2022.

[15] Sercel, C. L., "Characterization of Performance and Current Drive Mechanism for the Rotating Magnetic Field Thruster," Ph.D. thesis, University of Michigan, 2023.

[16] Gill, T. M., "Fundamental Limitations of Rotating Magnetic Field Thrusters," Ph.D. thesis, University of Michigan, 2024.

[17] Gill, T., Sercel, C. L., Zoppi, G., and Jorns, B., "A Comparative Study of Continuous-Wave and Pulsed Operation of Rotating Magnetic Field Thrusters for Plasma Propulsion," *AIAA SCITECH 2024 Forum*, 2024. https://doi.org/10.2514/6.2024-2706, URL https://arc.aiaa.org/doi/abs/10.2514/6.2024-2706.

[18] Gill, T. M., Sercel, C. L., and Jorns, B. A., "Experimental Investigation into Mechanisms for Energy Loss in a Rotating Magnetic Field Thruster," *37th International Electric Propulsion Conference*, 2022. URL https://pepl.engin.umich.edu/pdf/IEPC-2022-Gill.pdf.

[19] Zoppi, G., Gill, T. M., Sercel, C. L., and Jorns, B. A., "Efficiency Mode Analysis of a Continuous Wave Rotating Magnetic Field Thruster Informed by a Validated Fluid Model," *38th International Electric Propulsion Conference*, 2024. URL https://pepl.engin.umich.edu/pdf/Zoppi_IEPC_2024.pdf.

[20] Jameson, K. K., "Investigation of hollow cathode effects on total thruster efficiency in a 6 kW Hall thruster," Ph.D. thesis, 2008.

[21] Mikellides, I., Katz, I., Hofer, R., and Goebel, D., *Design of a Laboratory Hall Thruster with Magnetically Shielded Channel Walls, Phase III: Comparison of Theory with Experiment*, 2012. https://doi.org/10.2514/6.2012-3789, URL https://arc.aiaa.org/doi/abs/10.2514/6.2012-3789.

[22] Sekerak, M. J., "Plasma Oscillations and Operational Modes in Hall Effect Thrusters," Ph.D. thesis, University of Michigan, 2014.

[23] "Flexible Ferrite Sheet Datasheet," Tech. rep., Fair-Rite Products Corporation, n.d.

[24] "Power LDMOS Transistor Product Datasheet," Tech. rep., Ampleon, 2015.

[25] Goebel, D. M., and Katz, I., *Fundamentals of Electric Propulsion: Ion and Hall Thrusters*, Jet Propulsion Laboratory, 2008.

[26] Chen, F. F., *Introduction to Plasma Physics and Controlled Fusion*, 3rd ed., Springer, 2008.